Hard-Template preparation of Au/CeO2 mesostructured catalysts and their activity for the selective oxidation of 5-hydroxymethylfurfural to 2,5-furandicarboxylic acid

28 November 2024

Hard-template preparation of Au/CeO$_2$ mesostructured catalysts and their activity for the selective oxidation of 5-hydroxymethylfurfural to 2,5-furandicarboxylic acid

Alice Lolli[a,c], Rossella Amadori[a], Carlo Lucarelli[d], M.Giorgia Cutrufello[b], Elisabetta Rombi[b], Fabrizio Cavani[a,c], Stefania Albonetti[a,c*]

[a]Università di Bologna, Dipartimento di Chimica Industriale "Toso Montanari", viale Risorgimento, 4 - 40136 Bologna, Italy

[b] Università di Cagliari, Dipartimento di Scienze Chimiche e Geologiche, Complesso Universitario di Monserrato, S.S. 554 bivio Sestu - 09042 Monserrato (CA), Italy

[c]Consorzio INSTM – UdR Bologna, Via G. Giusti, 9 - 50121 Firenze, Italy

[d]Università dell'Insubria, Dipartimento di Scienza e Alta Tecnologia, Via Valleggio, 11 - 22100 Como, Italy

* Corresponding author: Phone: +390512093681 – Fax: +390512093679 – E-mail address: stefania.albonetti@unibo.it

ABSTRACT

Ordered mesoporous CeO$_2$ has been prepared via a hard-template method using SBA-15 as a structure-directing agent. Leaching with NaOH and thermal treatment at 500°C enabled the removal of the inorganic template, thus resulting in the formation of long-range ordered CeO$_2$. Nevertheless, small amounts of silica were present in final oxides. The resulting CeO$_2$ samples were used as supports for Au nanoparticles and the prepared catalysts were tested in the selective oxidation of 5-hydroxymethylfurfural

(HMF) to 2,5-furandicarboxylic acid (FDCA). Fine tuning of the silica template removal process was necessary to prepare active materials, by maximizing the close contact between the metal and the support, and thus confirming the important role of ceria defects in 5-hydroxymethylfurfural oxidation to 2,5-furandicarboxylic acid.

1. Introduction

CeO$_2$ is considered one of the most important oxides used as a support for metal-based catalysts in oxidation reactions. Cerium oxide is able to oxidize a molecule, by releasing oxygen atoms. This process leaves two localized electrons on the surface which are then transferred to the nearby cerium atom, thus promoting its reduction (Ce^{4+} → Ce^{3+}) [1]. For instance, its redox and oxygen storage capacity (OSC) properties are responsible for many catalytic reactions such as CO [2,3], VOCs, and alcohols oxidation [4,5].

Cerium oxide catalytic activity is strictly correlated to its reducibility, oxygen storage capacity, and the presence of oxygen vacancies. These peculiar characteristics are mainly due to particle size distribution, crystalline structure, and surface defect sites. However, it is a very well-known fact that these properties are strictly dependent on structural features, which are mainly influenced by the preparation method. It is therefore necessary to study some suitable synthetic strategies in order to be able to obtain samples with tuned particle size, surface area, reducibility, and OSC [6]. As far as defect sites are concerned, Overbury and coworkers [7] demonstrated by Raman spectroscopy that the Frenkel-type oxygen defects present on the oxidized ceria are

more abundant in nanorods than in nano-octahedra, where they are negligible. The presence of these defective sites led to the formation of different surface oxygen atoms, which influenced the catalytic activity for the selective oxidation of aldehydes to carboxylic acids, due to the changed interaction of the substrate with the catalyst [8].

Moreover, not only defect sites, but the preferential exposure of a crystal plane and crystal morphologies also, can deeply affect catalytic performances. The use of nanocrystalline cerium oxide has actually been shown to promote oxygen mobility. Corma and coworkers [5] reported an enhancement in the aerobic oxidation of alcohols when using cerium oxide nanoparticles instead of a conventional support for gold-based catalysts. They have also shown how cerium oxide took part in the reaction, by creating a synergistic effect with the gold deposited on its surface. The presence of nanoparticulate cerium oxide has revealed superior properties even in aldehyde oxidation in the liquid phase, while a very similar catalytic behavior was achieved using mesoporous cerium oxide [9].

In order to obtain oxides with specific morphology and precise exposed crystalline domain, many researchers have developed different synthetic strategies [8,10]. In the field of catalyst preparation and material science, mesostructured materials have attained an important role, since they are characterized by a high surface area and pore volume, great resistance to thermal and hydrothermal treatments, and shape selectivity. Suitable methods for the synthesis of mesoporous rare-earth metal oxides have been developed [11]. Among them, the hard-template technique must be preferred, since it permits the formation of long-range ordered mesoporous materials which preserve their typical structure even after calcination treatment [12,13].The hard-template technique involves the use of a mesostructured solid as template for the growth

of the guest metal oxide, from an appropriate molecular precursor. Such growth is confined within the pore system of the template, which can then be removed (by leaching, for instance), thus leaving the guest replica of the topological structure of the host. Typically, hard-templated oxides can be prepared using mesostructured silicas – namely SBA-15 [14,15], KIT-6 [2,15], and MCM-48 [16] – as templates.

Since the morphology of the system seems to be essential for fostering the catalytic activity, we synthesized hard-templated cerium oxide samples with a controlled morphology, to be used as supports for pre-formed gold nanoparticles. Metal nanoparticles were prepared using a simple and easily reproducible synthetic approach, which made it possible to compare the different catalysts obtained using different cerium oxides as supports. After a deep characterization, the obtained catalysts were tested in the liquid-phase selective oxidation of 5-hydroxymethylfurfural (HMF).

As a matter of fact, CeO_2-supported gold catalysts have been found to be very active for CO [17], VOCs [18,19], alcohol [20], and aldehyde [21] oxidation reactions. The oxidation of HMF to 2,5-furandicarboxylic acid (FDCA) has attracted the interest of researchers [22,23], since it allows the transformation of a biomass derivative into a starting material for the production of polymers which are alternative to those obtained from fossil-based raw materials. With this aim, Au/CeO_2 catalysts have been found to be very efficient for HMF oxidation in the liquid phase under basic conditions [24,25]. However, since the activity of such catalysts is strictly correlated to defect formation, redox properties, and gold-support interactions [26], the use of supports with high surface areas and regularly-shaped mesopores seems to be worthy of investigation.

2. Experimental

2.1. Synthesis

2.1.1. CeO$_2$ supports

SBA-15 mesostructured silica was prepared as previously reported by Zhao et al. [27] (see Supplementary Material for details – Figures S1-S3) and used as the template in the synthesis of CeO$_2$ supports.

7.6 g of Ce(NO$_3$)$_3$·6H$_2$O (Fluka, $\geq$ 99.0%) were dissolved in 25 cm^3 of ethanol (Sigma-Aldrich, absolute, $\geq$ 99.8%). 1 g of SBA-15 was then added to 15 cm^3 of the obtained solution and the suspension was stirred at room temperature for 1 h. Next, the solvent was evaporated at 60°C overnight, and the impregnation step was then repeated with the aim of filling the SBA-15 pores completely. The resulting solid was subsequently transferred to a furnace and calcined at 500°C for 3 h to let nitrates decompose into the corresponding oxides. The SBA-15 template was then removed by leaching with a solution (2M) of NaOH (Sigma-Aldrich, $\geq$ 98%, pellets) at 50°C. Lastly, the resulting material was washed up to pH 7 with distilled water, dried at 60°C for 12 h and then calcined at 500°C under static conditions for 3 h. The resulting material was named CeO$_2$_a. Additional CeO$_2$ supports, named CeO$_2$_b and CeO$_2$_c, were also obtained by repeating the leaching process and the following steps of washing, drying, and calcination for one or two more times, respectively.

2.1.2. Gold nanoparticles

Gold nanoparticles were prepared using a previously described method [28, 29]. In brief, appropriate amounts of poly(vinylpyrrolidone) (PVP K25, approx. 29,000 MW, Sigma Aldrich), used as nanoparticle stabilizers, and of an aqueous solution of NaOH were mixed and heated at 95°C. At this temperature, β-D-Glucose (Fluka, 99.9%) and an aqueous solution containing the metal precursor (HAuCl$_4 \cdot$3H$_2$O, Sigma Aldrich, 99.999%) was added and the solution was kept under stirring for 2.5 min. The ratio among PVP, β-D-glucose, NaOH, and metal was optimized with respect to gold content in previous studies [30-32]: PVP/Au = 2.75, NaOH/Au = 8, and Glucose/Au = 2 molar ratios. The formation of gold nanoparticles was indicated by the red color of the resulting sol (final Au concentration = 0.005 mol L^{-1}). Prepared sols were analysed by Uv-vis, Dinamic Ligh Scattering (DLS) and XRF analysis to evaluate the reproducibility of our preparation. More detailed data on sols preparation and characterization were reported in our previous work [30-32].

Prior to use, the prepared sols were concentrated with 50 kDa Amicon Ultra filters (Millipore) to remove the excess of PVP and other reagents dissolved in the reaction medium and to reach the necessary volume for incipient wetness impregnation.

2.1. Catalyst preparation

Catalysts were prepared by the incipient wetness impregnation of mesostructured CeO$_2$ supports and of a commercial CeO$_2$ (Ceria 60 Evonik) with the colloidal dispersion of gold nanoparticles. After the impregnation step, the obtained catalysts were dried at 120°C overnight and then calcined at 300°C for 3 h in order to remove PVP, which was

found to be necessary for enhancing the catalytic activity [26]. All the catalysts were prepared with a gold loading of 1.5 wt%.

2.2. Characterization techniques

The textural analysis was carried out with an ASAP 2020 analyzer (Micromeritics), determining the nitrogen adsorption/desorption isotherms at -196°C. Before analyses, samples were heated overnight under a vacuum up to 250°C (heating rate, 1°C min^{-1}).

A wavelength dispersive X-Ray Fluorescence Spectrometer (Panalytical Axios Advanced), equipped with Rh anode as the X-Ray source, was used to check the presence of residual SiO_2 on CeO_2 supports after removing the SBA-15 template. Measurements were carried out – under vacuum – on samples in the form of pellets prepared by adding 100 mg of an organic wax to 300 mg cerium oxide.

Small-angle XRD analyses were performed on a Seifert X3000 diffractometer with a θ-θ Bragg-Brentano geometry with Cu-Kα wavelength (λ = 1.5418 Å). Samples were analyzed in the 0.8° - 2.5° 2θ range, counting for 20 s at each 0.01° step.

Wide-angle XRD measurements were carried out at room temperature with a Bragg-Brentano diffractometer (X'pertPro PANalytical) equipped with a fast X'Celerator detector, using a Cu anode as the X-Ray source. Supports and catalysts were analyzed in the 2θ region 20° - 65° and 10° - 85°, respectively, counting for 20 s at each 0.05° step.

Transmission Electron Microscopy (TEM) observations were carried out using a FEI Tecnai F20 microscope equipped with a Schottky emitter and operating at 200 keV. The instrument was equipped both with a Fischione High Angle Annular Dark Field

Detector (HAADF) for Scanning Transmission Electron Microscopy (STEM) investigations and with an Energy Dispersive X-Ray spectrometer (EDX) for X-Ray microanalysis. Finely ground samples were dispersed in isopropanol and subjected to an ultrasonic bath. Suspensions were then dropped onto a holey carbon film and dried for observation.

TPR profiles were recorded on a TPD/R/O 1100 apparatus (ThermoQuest), under the following conditions: sample weight, 0.1 g; heating rate (from 60 to 650°C, then hold for 30 min), 20°C min^{-1}; flow rate, 20 cm^3 min^{-1}; H$_2$, 5 vol% in Ar. Hydrogen consumption was monitored by a thermal conductivity detector (TCD). A molecular-sieve trap was placed before entering the detector, in order to eliminate the contribution of water (formed during the reduction process) in the TCD signal. Prior to the experiment, samples were pretreated for 30 min in an O$_2$ (5 vol%)/He mixture (20 cm^3 min^{-1}) at 120°C and 300°C for the dried and calcined Au/CeO$_2$ catalysts, respectively.

2.3. Catalytic activity experiments

HMF oxidation reactions were performed in a 100 mL autoclave reactor, equipped with a mechanical stirrer (0-600 rpm) and pressure and temperature measurement gauges. HMF (0.078 mol L^{-1}), catalyst, and NaOH (with HMF/metal/NaOH molar ratio equal to 1:0.01:4) were added to 25 cm^3 of distilled water and poured into the reactor. After purging three times with O$_2$ (5 bar), the reactor was pressurized at 10 bar, heated up to 70°C, and kept under stirring (400 rpm) for 4 h. Then, after cooling down to room temperature, the final reaction mixture was recovered and diluted for HPLC analysis with an Agilent 1260 Infinity, equipped with an Aminex HPX-87H 300 mm x 7.8 mm

column, using a 0.005 M H$_2$SO$_4$ solution in water as mobile phase. Product identification and quantification were achieved by calibration with commercial reference samples.

3. Results and Discussion

3.1. CeO$_2$ synthesis and characterization

Mesostructured CeO$_2$ was prepared using the hard-template method according to the previously described procedure. This nanocasting process makes it possible to replicate the morphology of the SBA-15 template in the reverse form. The calcination of mesoporous silica impregnated with cerium salt leads to the formation of crystalline ceria inside the SBA-15 pores; then the silica framework can be dissolved by NaOH treatment. The removal of the silica template, which probably has oxygen linkages with ceria, may produce structural defects. Moreover, the further calcination of the solid after the leaching step was reported to have a positive effect on the crystallinity and stability of the materials [16]; nevertheless, a high temperature treatment may also cause a significant decrease in the number of corner and edge sites [16, 33] as well as in the concentration of oxygen vacancies [34], whose presence can positively affect the catalytic activity. For these reasons, the pivotal role of the template-leaching process in the formation of the mesostructured CeO$_2$ support has been thoroughly investigated by performing a different number of template-removal cycles.

Wide-angle XRD patterns of the synthesized CeO$_2$ materials (Figure 1) show peaks at 2θ values of 28.6, 33.1, 47.5, and 56.4°; these can be ascribed to the (111), (200), (220), and (311) reflection lines of the face-centered cubic-phase fluorite-type

structure of cerium oxide (PDF card 81-0792), which indicate the formation of well crystallized materials regardless of the number of template-removal cycles used during the synthesis. The size of CeO_2 crystallites, calculated by the Scherrer equation, is in the 8-10 nm range for all samples.

Small-angle XRD results for CeO_2_a and CeO_2_b, obtained by a different number of leaching cycles, are shown in Figure 2. No significant differences were seen between the two patterns. Three signals, which can be indexed as the (100), (110), and (200) reflections characteristic of the hexagonal p6mm (2D-symmetry) structure, can be observed. However, the low intensity of the signals seems to indicate that the materials do not exactly replicate the original mesostructure of the SBA-15 template.

N_2 adsorption-desorption isotherms and the pore size distribution curves of the CeO_2 supports are shown in Figure 3. All samples exhibit a type IIb isotherm [35] with a hysteresis loop typical of mesoporous solids (Figure 3a-c). Surface area, S.A., was calculated through the BET equation. The BJH method was applied to the desorption branch of the isotherms to obtain pore size distribution curves (Figure 3d-f). Textural results are summarized in Table 1. Hard-templated CeO_2 supports exhibit surface area in the range 103-121 m^2 g^{-1}, much higher than that of the commercial cerium oxide (53 m^2 g^{-1}). The obtained values are comparable with those reported in the literature for similar materials [36,37]. These values seem to decrease slightly with the increase in the number of template-removal cycles. All the hard-templated samples show a bimodal distribution of the pore size, with a first peak centered at around 3.2 nm and a second broad peak centered at around 9 nm. The former contribution, whose pore size value is consistent with the pore wall thickness of the parent SBA-15 (see Supplementary Material), is responsible for the moderate change in slope observable at p/p_0 ranges of

0.3-0.6 in the N_2 physisorption isotherms. Such contribution seems to suggest that the topological structure of the template is replicated to some extent in the prepared CeO_2 samples. However, the presence of the second contribution, indicative of larger pores with a broad size distribution, suggests that the structure of the obtained materials is partially disordered.

TEM images of CeO_2_a and CeO_2_b (Figure 4) clearly show the ordered rod-like morphology of the materials, with the oxide appearing as rods of ca. 8 nm in diameter arranged in a hexagonal array. However, regions in which structural collapse has occurred to some extent are also visible. By closely inspecting Figure 4, it can be seen that most of the channels are not exactly void replicas of the former walls of the SBA-15 host, being about 1-2 nm in diameter. This can likely be explained by two combined effects. The first is related to the non-filling of the SBA-15 micropores by cerium oxide, leading to the lack of "cross linkages" between the rods. Such bridges would stabilize the reverse moulded replica against structural collapse during the removal of the templating agent. The second effect is related to the possible structural rearrangement of the nanorods because of the calcination treatment after the removal of the SBA-15 template, when the particles growth is no longer inhibited by their confinement within the silica channels. Particles slightly larger (8 nm) than the pore size of the SBA-15 template (6-7 nm) have actually been observed by TEM for both CeO_2_a and CeO_2_b supports.

XRF analyses have been carried out on the prepared ceria supports to check the presence of residual silica. The results reported in Table 1 show that small amounts of SiO_2 remained in all the synthesized samples, suggesting that complete removal of the template is a very demanding task. By performing the template-removal process twice

(CeO$_2$_b), it was possible to reduce the residual amount of silica which, however, remained constant after another leaching-calcination cycle (CeO$_2$_c).

3.2. Au-supported catalysts

Nanoparticle homogeneity is of crucial importance in the study of the nature and effect of the interactions between the metal and the support oxide. In this field, size-controlled Au nanoparticles, whose particle size is established, were prepared to enhance the properties of nanostructured ceria [26]. Indeed, the deposition of preformed nanoparticles is not generally support-dependent, making it possible to investigate the effect of the support on the reaction, thanks to the minimal influence of the support in determining the size and dispersion of the active phase. Therefore, the studied catalysts were obtained by immobilization on mesostructured CeO$_2$ surface of preformed gold colloid prepared by the reduction of HAuCl$_4$ with β-D-glucose in the presence of PVP as the stabilizer in water. This synthesis resulted in a stable colloidal suspension with a mean particle size of around 4-5 nm (Figure 5).

The obtained sol was deposited onto CeO$_2$_a and CeO$_2$_b mesostructured supports; CeO$_2$_c material (which exhibits structural and textural properties and residual silica content very similar to those of CeO$_2$_b) will be no longer considered in the discussion. Nevertheless, the obtained data on this material confirms CeO$_2$_b ones, evidencing the reliability of the obtained results. Au supported on commercial ceria (Au/CeO$_2$) was also prepared for comparison (Figures S4-S6).

Textural properties of the ceria samples were not affected by either the gold nanoparticles deposited on the surface or by the deposition procedure. Indeed, the surface area of all the mesostructured materials, either dried at 120°C or calcined

300°C, remains close to 110 m^2 g^{-1} (Table 2). The slight increase in surface area observed for calcined samples maybe reasonably due to the elimination of PVP, which surrounded the nanoparticles and may occlude oxide porosity.

As expected, after immobilization and calcination, the mesostructured morphology of ceria was preserved in all cases, as clearly shown by micrographs in which the ordered rod-like structure of the materials predominated (Figures 6 and 7). The absence of significant changes in the support structure during sol immobilization was also confirmed by XRD patterns (Figure 8) which clearly show the main reflection peaks belonging to cerium oxide.

The peculiarity of gold catalysis using ceria as the support is the synergic effect that causes the increase in CeO$_2$ oxygen storage capacity, fostering the superficial Ce^{4+} reduction. For this reason, the interaction between gold nanoparticles and the oxide is fundamental, and is governed by the relative dimension of the two actors and their surface properties.

In the case of gold nanoparticles immobilized on mesostructured ceria, the above-mentioned peculiarity was studied by determining, first of all, the morphology and distribution of gold and, afterwards, the nature of the interaction with support by using reactive techniques.

Metal particle size was determined by HRTEM (Table 2). This technique highlighted the presence of small particles in both mesostructured catalysts. After deposition, in the case of both dried and calcined samples, an important increase in particle size was seen. Most of the gold particles, larger than ceria crystallites, proved to be randomly deposited on the oxide surface without a particular tendency to be linked over ceria nanorods.

The results obtained show a significant difference between the size and distribution of pristine gold nanosol and metal nanoparticles supported on mesoporous CeO_2. Indeed, while pristine gold shows well-defined, rather spherical metal nanoparticles with a relatively low polydispersity and diameter distribution centered at 4.4 nm (Figure 5), a significant increase in particle size and distribution was observed after the impregnation and drying steps (Figure 6a and 7a). This effect is unusual for samples prepared by preformed nanoparticles and was not evident when using commercial cerium oxide, which permits the preparation of samples with a rather narrow gold particle size distribution, similar to that of the sol [26] (see Supplementary Material, Figure S5).

Furthermore, some significant modifications are evident after the thermal treatment at 300°C for the sample which is characterized by higher silica content (Figure 6b). TEM images show a remarkable tendency of preformed gold nanoparticles to reorganize on the support while the sintering trend seems to be correlated with the silica content in the material. Indeed, the statistical analysis of TEM images for calcined Au/CeO_2_a indicates a metal diameter distribution centered at 13 nm and a high polydispersity (Figure 6). The distribution of the particle diameter was evenly spread out in the 4-24 nm range, meaning that Au nanoparticles were very inhomogeneous in size. Conversely, gold nanoparticles present on Au/CeO_2_b sample were not strongly affected by calcination (Figure 7b). Even in this case, the distribution profile changed slightly, moving from the dried to the calcined sample, while some large Au nanoparticles (approx. 16 nm) formed after the thermal treatment, leading to a bimodal gold particle size distribution. Nevertheless, the average particle growth was not very significant, and the metal nanoparticle size was almost the same obtained using the

commercial support (Figure S5). These results suggest a possible correlation between gold dispersion on the mesostructured CeO_2 and the presence of residual silica from hard-template preparation on the support surface. This effect was already observed on samples after drying, where we found a wide particle size distribution, which is generally not observed on Au/CeO_2 prepared by preformed nanoparticles [26]. Although it is well known that gold clusters are characterized by high mobility, and considering the fact that the interaction between gold and silica is weak [38,39], the presence of small amounts of silica on the ceria surface can strongly affect gold mobility during deposition and thermal treatments. Therefore, the structure of gold supported on mesoporous ceria obtained using SBA-15 as the template will strongly depend on the residual silica present on materials.

It is very well known that, in the presence of gold, the oxygen storage capacity of reducible oxides such as CeO_2 may increase, facilitating the superficial Ce^{4+} reduction. Thus the chemical effects of gold deposition on mesostructured ceria were investigated using H_2-TPR. Typically, the TPR profile of pristine CeO_2 is characterized by reduction peaks at 450-500°C and 800°C which may be ascribed to both the surface capping oxide ions and the bulk oxygen, respectively [40-42]. H_2-TPR profiles of Au/CeO_2_a and Au/CeO_2_b catalysts are shown in Figure 9. All sample profiles show the presence of intense reduction peaks at temperatures well below 500°C. This confirms the interaction of gold with the support, leading to the formation of highly reducible ceria species. Indeed, it is reported that gold can cause a reduced strength of the surface Ce–O bonds adjacent to metal atoms, thus leading to a higher surface lattice oxygen mobility and, therefore, to a higher reactivity of these oxygen species [43]. By analyzing the TPR profiles of prepared samples more in detail and comparing the results

obtained in literature and with gold supported on commercial ceria (Figure S6), several important aspects maybe highlighted. The TPR profiles of dried Au/CeO$_2$_a and Au/CeO$_2$_b (Figure 9) are very similar as for onset temperatures, shape of reduction peaks, and reduction temperatures. It should be taken into account that this analysis is affected by the presence of the organic stabilizer (polyvinylpyrrolidone) used during sol synthesis and still present over nanoparticle surface after drying. Indeed, TGA-DTA thermal analysis made on these samples demonstrated that, under air flow, PVP is completely burned off at 300°C [26]. The presence, in the reducing gaseous mixture, of organic species deriving from the thermal decomposition of PVP is most probably responsible for the appearance of the negative signal at temperatures between ca. 400 and 500°C in the TPR profiles of dried Au/CeO$_2$_a and Au/CeO$_2$_b (Figure 9).

Samples calcination at 300°C significantly affected TPR profiles. The thermal treatment promoted PVP combustion, eliminating its interference in gold-support interaction [43,44] and fostering the general shift of the reduction temperature toward lower values. In addition, a significant difference between the reduction temperature of calcined Au/CeO$_2$_a and Au/CeO$_2$_b was highlighted. Indeed, the peak for Au/CeO$_2$_b shifted to a lower temperature (205°C) compared to Au/CeO$_2$_a (245°C). The extent of the shift of the first reduction peak of pristine ceria to lower temperatures upon gold deposition is generally considered an indication of the strength of the interaction between gold and ceria. The present results indicate that such interaction is stronger over Au/CeO$_2$_b than over Au/CeO$_2$_a, and this trend might be correlated with the amount of residual silica present on ceria surface. Actually, according to XRD and TEM data, the presence of silica on Au/CeO$_2$_a did not allow the prevention of gold particle growth, thus decreasing gold capacity to activate the surface Ce^{4+} reduction. On the

contrary, Au/CeO$_2$_b, which was characterized by a lower silica amount and smaller gold particle size, also had a lower reduction temperature.

3.3 Catalytic properties

Prepared catalysts were tested in the liquid phase oxidation of 5-hydroxymethylfurfural (HMF) to 2,5-furandicarboxylic acid (FDCA)in order to verify the influence of the support on the catalytic activity. HMF has two groups that can be oxidized: the alcoholic and the aldehydic group. The complete or partial oxidation of one or both groups may lead to the formation of different products (Scheme 1). The reaction on Au-based catalysts has been generally described in two steps: (i) the aldehyde oxidation to 5-hydroxymethyl-2-furancarboxylic acid (HMFCA), and (ii) the oxidation of alcohol to FDCA, through the formation of 5-formyl-2-furancarboxylic acid (FFCA) as the reaction intermediate. 2,5-diformylfuran (DFF) was not observed in the course of the reaction with gold-base catalysts.
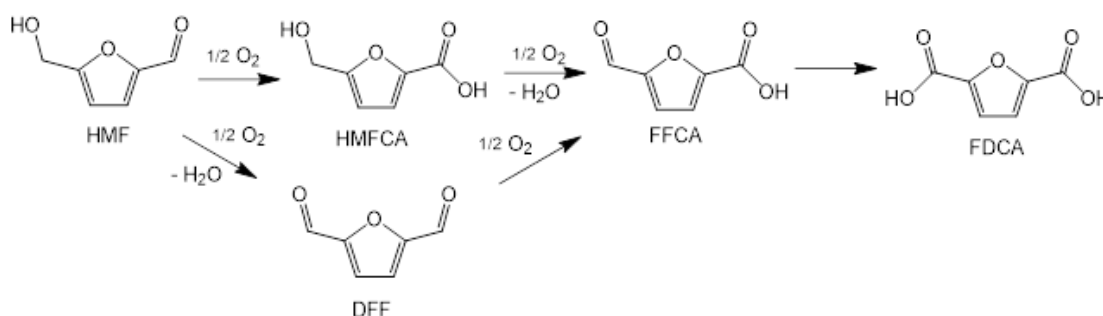
Scheme 1. General reaction pathway for HMF oxidation.

Our study indicated that pure ceria supports were inactive in the oxidation, while forming very small amounts of HMFCA and by-products derived from HMF degradation. Conversely, the oxidation of HMF over Au-supported samples resulted in

17

the formation of both HMFCA and FDCA (Figure 10), while FFCA was never observed in our reaction conditions. For all samples, after 4 h reaction time, HMF conversion was always complete, but significant differences were seen among catalysts in terms of product selectivity.

Dried Au/CeO$_2$_a catalyst exhibited a moderate activity in the liquid phase oxidation of HMF. FDCA yield reached 38% after 4 h, while the main product was the intermediate HMFCA. The selectivity toward FDCA increased significantly for Au/CeO$_2$_b, containing a lower amount of residual silica, due to the faster oxidation of HMFCA which, after 4h, led to FDCA yield of 51%. In a discussion of the reasons for the different behaviors shown by the two mesostructured CeO$_2$ supported samples, it must be stressed that CeO$_2$ is known to be an excellent redox support for gold, owing to the high number of oxygen vacancies and the easy Ce^{4+}/Ce^{3+} redox transition, with both significant oxygen mobility and storage capacity. Nevertheless, several works [45,46] have demonstrated that all these events are strongly dependent on Au-CeO$_2$ interfacial interaction, while the presence of some substances on ceria/gold interfaces, such as silica or PVP, may interfere with the process, decreasing the catalytic activity of materials. Considering that SiO$_2$ is not characterized by significant bulk and surface oxygen mobility and that silica impurity may decrease Au-CeO$_2$ interaction and oxygen conductivity [47], the presence of different quantities of this oxide, spread over the ceria surface on Au/CeO$_2$_a and Au/CeO$_2$_b samples, may be the reason for different performances. Indeed, the two catalysts have very similar morphology, surface area, and gold size distribution, and these properties cannot be responsible for the different FDCA yield.

Since catalysts were synthesized by using PVP-stabilized gold, CeO_2-supported gold samples were thermally treated to examine the effect of PVP removal on mesoporous systems. Previous results on ceria-supported catalysts [26] demonstrated that the PVP presence over Au nanoparticles decreased their catalyst activity in HMF oxidation.

To obtain clean metallic species, Au/CeO_2_a and Au/CeO_2_b were calcined at 300°C. TEM results (Figure 7) demonstrated that the Au/CeO_2_b sample almost retained gold size (the mean particle size was 7 nm, versus 6 nm obtained with the dried sample) while Au/CeO_2_a showed a considerable sintering phenomenon leading to very broad gold size distribution (Figure 6).

The thermal treatment of Au/CeO_2_a significantly decreased its catalytic activity while FDCA formation was totally prevented (Figure 10); in addition, by-products derived from HMF degradation were detected in high amounts. It is well known that HMF degradation takes place when the catalyst is not able to suddenly catalyze HMF oxidation [48]. This degradation is very common in the presence of a base even at ambient temperature, leading to the formation of a dark brownish reaction mixture. Therefore Au/CeO_2_a catalyst, after calcination, was unable to rapidly convert HMF to HMFCA, thus permitting the fast decomposition of this molecule.

The agglomeration of metal nanoparticles with calcination, together with the associated decrease in the interaction with ceria mesostructured supports, might cause the observed decrease in FDCA yield. However, recent data has demonstrated that large Au particles (size > 20 nm) are able to oxidize HMF with high selectivity, if a suitable interaction with the ceria support is guaranteed [26,49]. Thus, the weak gold-support interactions could be the main reason for the very low activity of calcined Au/CeO_2_a.

Conversely, the calcination of Au/CeO_2_b, with optimized template removal, significantly boosted the activity; indeed, FDCA selectivity over this sample increased from 51% to 92%. These data confirm previous results on Au/CeO_2 catalysts, demonstrating the importance of PVP elimination in activating mesoporous catalysts, by maximizing the contact between the metal and the support, and thus suggesting an important role of ceria defects on 5-hydroxymethylfurfural oxidation to 2,5-furandicarboxylic acid.

In light of the results of the activity measurements, dried and calcined Au/CeO_2_b was selected for a study of the effect of reaction time on catalytic performance. Figures 11A and 11 B show HMF conversion and product selectivity as a function of reaction time. On both catalysts, HMFCA formation was very fast under the conditions used, and the complete transformation of HMF to HMFCA was obtained after few minutes. During the first 30 minutes, the main product was HMFCA. Results indicate that the reaction network consists of the direct and rapid transformation of HMF into HMFCA, while the rate-determining step for FDCA production is the oxidation of the hydroxymethyl group of HMF. Other by-products, such as FFCA and DFF, were not detected, and after 4 h of reaction time, a FDCA selectivity of 51% was obtained for dried sample and 92% for calcined one. These results demonstrated that the fine tuning of the silica template removal over hard-templated ceria might reduce the quantity of residual silica in the final material, thus controlling its effect on gold dispersion and gold-CeO_2 interaction.

4. Conclusions

Mesostructured CeO$_2$ was successfully prepared by nanocasting using mesostructured silica SBA-15 as a hard template. Compared to commercial ceria, the prepared materials exhibited a controlled morphology and were characterized by small crystallites and high surface area. Gold metal nanoparticles with well-defined size were immobilized on prepared oxides to explore the role of support morphology in the oxidation of HMF. Since obtained Au nanoparticles were, in the majority, larger than the pores between rods in hexagonal arrangement, the metal was predominantly deposited on the outer surface of such arrays of rods, limiting the effect of the specific morphology on the final catalyst. Nevertheless obtained results permitted to highlight the main parameters affecting the hard-template preparation of Au/CeO$_2$ mesostructured catalysts. Indeed, the residual silica present on the hard-templated ceria surface after template removal was demonstrated to strongly affect gold nanoparticle deposition and growth during thermal treatments, making it difficult to discriminate among the various effects, i.e. the influence of particle size, phase segregation, and metal-oxide interaction. The fine tuning of the silica template removal process made it possible to limit the residual silica in the final material, thus reducing its negative effect on gold dispersion and Au-CeO$_2$ interaction. Au nanoparticles supported on optimized mesostructured ceria were demonstrated to be efficient catalysts for the aerobic oxidation of HMF to FDCA, thus suggesting the potential use of hard-templated mesoporous ceria in selective oxidation processes. The calcination of Au/CeO$_2$ sample obtained by an optimized template removal procedure, significantly increased FDCA formation, confirming the importance of PVP elimination in order to develop a more active catalyst.

Acknowledgements

References

[1] M. Nolan, S. C. Parker, G. W. Watson, Surf. Sci. 595 (2005) 223-232.

[2] A. Trovarelli, Catalysis by ceria and related materials, Imperial College Press, U.K. 2002.

[3] O. A. Gonzalez Vargas, J. A. de los Reyes Heredia, A. Montesinos Castellanos, L. F. Chen, J. A. Wang, Mater. Chem. Phys. 139 (2013) 125-133.

[4] N. Pal, E.-B. Cho, D. Kim, RSC Adv. 4 18 (2014) 9213-9222.

[5] A. Abad, P. Concepcion, A. Corma, H. Garcia Angew, Chem. Int. Ed. 44 (2005) 4066-4069.

[6] G.Y. Adachi, T. Masui in A. Trovarelli (Ed), Catalysis by Ceria and Related Materials, Imperial College Press, 2002, pp. 51-76.

[7] Z. L. Wu, M. J. Li, J. Howe, H. M. Meyer, S. H. Overbury, Langmuir 26 (2010) 16595-16606.

[8] A. Corma, M. E. Domine, Chem. Commun. (2005) 4042-4044.

[9] Z. Qiao, Z. Wu, S. Dai, ChemSusChem 6 (2013) 1821-1883.

[10] J. G. Lv, Y. Shen, L. M. Peng, X. F. Guo, W. P. Ding, Chem. Commun. 46 (2010) 5909-5911.

[11] D. Gu, F. Schuth, Chem. Soc. Rev. 43 (2014) 313-344.

[12] P. Yang, D. Zhao, D. I. Margolese, B. F. Chmelka and G. D. Stucky, Nature 396 (1998) 152-155.

[13] A. Sayari and P. Liu, Micropor. Mesopor. Mater. 12 (1997) 149-177.

[14] Y. Ke, S.-Y. Lai, Micropor.Mesopor. Mater. 198 (2014) 256-262.

[15] S. C. Laha, R. Ryoo, Chem. Commun. (2003) 2138-2139.

[16] F. Ying, S. Wang, C-T. Au, S-Y. Lai, Micropor. Mesopor. Mater. 142 (2011) 308-315.

[17] M. Lopez, R. Arenal, B. Puertolas, A. Mayoral, S. H. Taylor, B. Solsona, T. Garcia, J. Catal. 317 (2014) 167-175.

[18] C. Gennequin, M. Lamallem, R. Cousin, S. Siffert, F. Aissi, A. Aboukais, Catal. Today 122 (2007) 301-306.

[19] R. Bonelli, S. Albonetti, V. Morandi, L. Ortolani, P. M. Riccobene, S. Scirè, S. Zacchini, App. Catal. A: Gen. 395 (2011) 10-18.

[20] M. Alhumaimess, Z. Lin, W. Weng, N. Dimitratos, N.F. Dummer., S.H. Taylor, J.K. Bartley, C. J. Kiely, G.J. Hutchings, ChemSusChem 5 (2012) 125-131.

[21] J. Beckers, G. Rothenberg, Green Chem. 12 (2010) 939-948.

[22] R.J. van Putten, J.C. van der Waal, D. de Jong, C.B. Rasrendra, H.J. Heeres, J.G. deVries, Chem. Rev. 113 (2013) 1499-1597.

[23] J. Zhang, J. Li, Y. Tang, L. Lin, M. Long, Carbohydrate Polymers 130 (2015) 420-428.

[24] O. Casanova, S. Iborra, A. Corma, ChemSusChem 2 (2009) 1138-1144.

[25] O. Casanova, S. Iborra, A. Corma, J. Catal. 265 (2009) 109-116.

[26] S. Albonetti, A. Lolli, V. Morandi, A. Migliori, C. Lucarelli, F. Cavani, Appl. Catal. B: Environ. 163 (2015) 520-530.

[27] D. Zhao, Q. Huo, J. Feng, B. F. Chmelka, G. D. Stucky, J. Am. Chem. Soc. 120 (1998) 6024-6036.

[28] P. Raveendran, J. Fu, L. Wallen, Green Chem. 8 (2006) 34-38.

[29] M. Blosi, S. Albonetti, M. Dondi, G. Baldi, A. Barzanti, PCT/EP2010/052534.

[30] M. Blosi, S. Albonetti, G. Baldi, F. Gatti, M. Dondi, Dyes Pigments 94 (2) (2012) 355-362.

[31] S. Albonetti, M. Blosi, F. Gatti, A. Migliori, L. Ortolani, V. Morandi, G. Baldi, M. Dondi, Stud. Surf. Sci. Catal. 175 (2010) 621-624.

[32] M. Blosi, S. Albonetti, S. Ortelli, A. L. Costa, L. Ortolani, M. Dondi, New J. Chem. 38 (2014) 1401-1409.

[33] Y. J. Wang, J. M. Ma, M.F. Luo, P. Fang, M. He, J. Rare Earths 25 (2007) 58-62.

[34] W. Yuejnan, M. Jingnieng, L. Mengfei, F. Ping, H. Mai, J. Rare Earths 25 (2007) 58-62.

[35] F. Rouquerol, J. Rouquerol, K. Sing, Adsorption by powders and porous solids, Principles, methodology and applications, Academic Press, London (1999), ch. 13, pp. 440-441.

[36] Y. Wang, Y. Wang, J. Ren, Y. Mi, F. Zhang, C. Li, X. Liu, Y. Guo, Y. Guo, G. Lu, J. Solid State Chem. 183 (2010) 277-284.

[37] S. Abdollahzadeh-Ghom, C. Zamani, T. Andreu, M. Epifani, J. R. Morante, Appl. Catal. B: Environ. 108-109 (2011) 32-38.

[38] M. P. Casaletto, A. Longo, A. M. Venezia, A. Martorana, A. Prestianni, Appl. Catal. A: Gen. 302 (2006) 309-316.

[39] S. Martínez-González, A. Gómez-Avilés, O. Martynyuk, A. Pestryakov, N. Bogdanchikova, V. Cortés Corberán, Catal. Today 227 (2014) 64-70.

[40] A. Trovarelli, G. Dolcetti, C. De Leitenburg, J. Kaspar, P. Finetti, A. Santoni, J. Chem. Soc. Faraday Trans. 88 (1992)1311-1319.

[41] S. Scirè, P. M. Riccobene, C. Crisafulli, Appl. Catal. B: Environ.101 (2010) 109-117.

[42] S. Mandal, C. Santra, K. K. Bando, O. O. James, S. Maity, D. Mehta, B. Chowdhury, J. Mol. Catal. A: Chemical 378 (2013) 47-56.

[43] S. Scirè, S. Minicò, C. Crisafulli, C. Satriano, A. Pistone, Appl. Catal. B: Environ. 40 (2003) 43-49.

[44] S. Scirè, P. M. Riccobene, C. Crisafulli, Appl. Catal. B: Environ. 101 (2010) 109-117.

[45] S. Carrettin, P. Concepción, A. Corma, J. M. L. Nieto, V. F. Puntes, H. Garcia, Angew. Chem., Int. Ed. 43 (2004) 2538-2540.

[46] D. Martin, D. Duprez, J. Phys. Chem. 100 (1996) 9429-9438.

[47] H. L. Tuller, Solid State Ionics 131 (2000) 143-157.

[48] H. A. Rass, N. Essayem, M. Besson, ChemSusChem 8 (2015) 1206-1217.

[49] H. Guo, A. Al-Hunaiti, M. Kemell, S. Rautiainen, M. Leskela, T. Repo, ChemCatChem 3 (2011) 1872-1875.

Tables

Sample	S.A. $(m^2 g^{-1})$	V_p $(cm^3 g^{-1})$	SiO_2 (wt%)
CeO_2_a	121	0.314	2.6
CeO_2_b	113	0.318	1.8
CeO_2_c	103	0.304	1.9

Table 1. Textural features and residual SiO_2 content of the synthesized mesostructured CeO_2 supports.

Sample	S.A. $(m^2 g^{-1})$	d_{HRTEM} (nm)
Au/CeO_2_a dried 120°C	110	7
Au/CeO_2_a calcined 300°C	113	13
Au/CeO_2_b dried 120°C	105	6
Au/CeO_2_b calcined 300°C	108	7

Table 2. Surface area and gold particle size from HRTEM analysis for the prepared catalyst.

Figure captions

Figure 1. WAXRD patterns of the mesostructured supports (CeO_2_a, CeO_2_b, CeO_2_c).

Figure 2. SAXRD patterns of the mesostructured sample CeO_2_a and CeO_2_b.

Figure 3. N_2 adsorption/desorption isotherms (a-c) and pore size distribution (d-f) of the mesoporous materials. Legend: (a,d) CeO_2_a, (b,e) CeO_2_b, (c,f) CeO_2_c.

Figure 4. HRTEM images of the sample CeO_2_a (a); CeO_2_b (b).

Figure 5. HRTEM image and particle size distribution of the gold nanoparticle suspension.

Figure 6. HRTEM images and Au particle size distribution for a) Au/CeO_2_a dried; b) Au/CeO_2_a calcined**.**

Figure 7. HRTEM images and Au particle size distribution for a) Au/CeO_2_b dried; b) Au/CeO_2_b calcined.

Figure 8. XRD patterns of the dried and calcined supported catalyst. Legend: a) Au/CeO_2_a dried, b) Au/CeO_2_a calcined, c) Au/CeO_2_b dried, d) Au/CeO_2_b calcined.

Figure 9. TPR profiles of the mesostructured catalysts: 1) Au/CeO_2_a dried, 2) Au/CeO_2_a calcined, 3) Au/CeO_2_b dried 4) Au/CeO_2_b calcined.

Figure 10. Product yields obtained with the dried and calcined mesostructured catalysts. Reaction conditions: 70°C, 10 bar O_2, HMF/metal/NaOH molar ratio 100:1:4, 240 minutes. Results are given at total conversion of HMF. Legend:■ FDCA yield, ■ HMFCA yield, ■by-products yield.

Figure 11. HMF conversion and product selectivity as a function of time on dried (A) and calcined (B) Au/CeO_2_b sample. Reaction conditions: 70°C, 10 bar O_2, HMF/metal/NaOH molar ratio 100:1:4. Legend: ♦HMF conversion, ■ HMFCA selectivity, ▲FDCA selectivity.
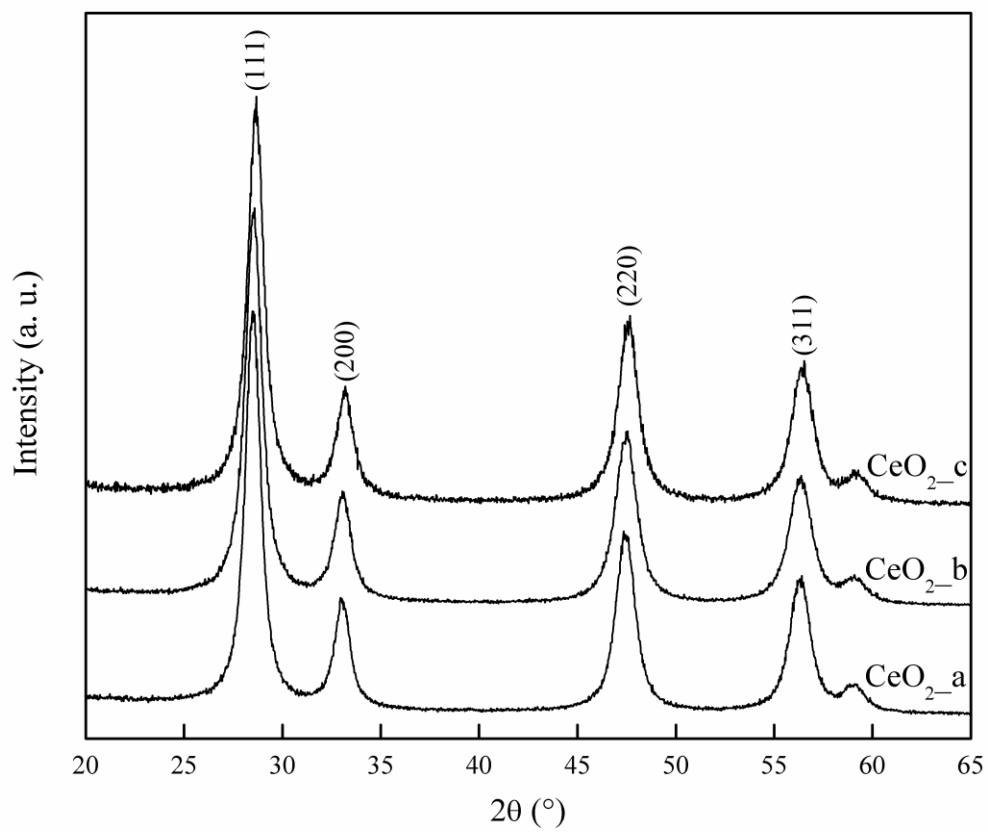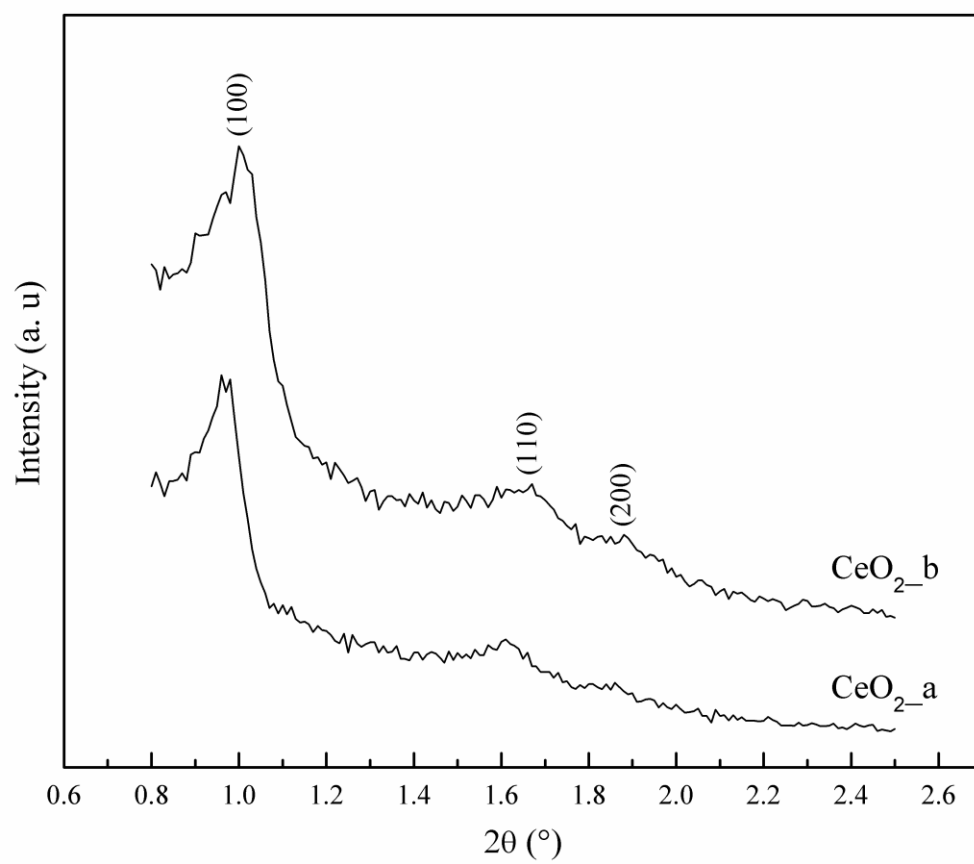
Figures

Figure 1
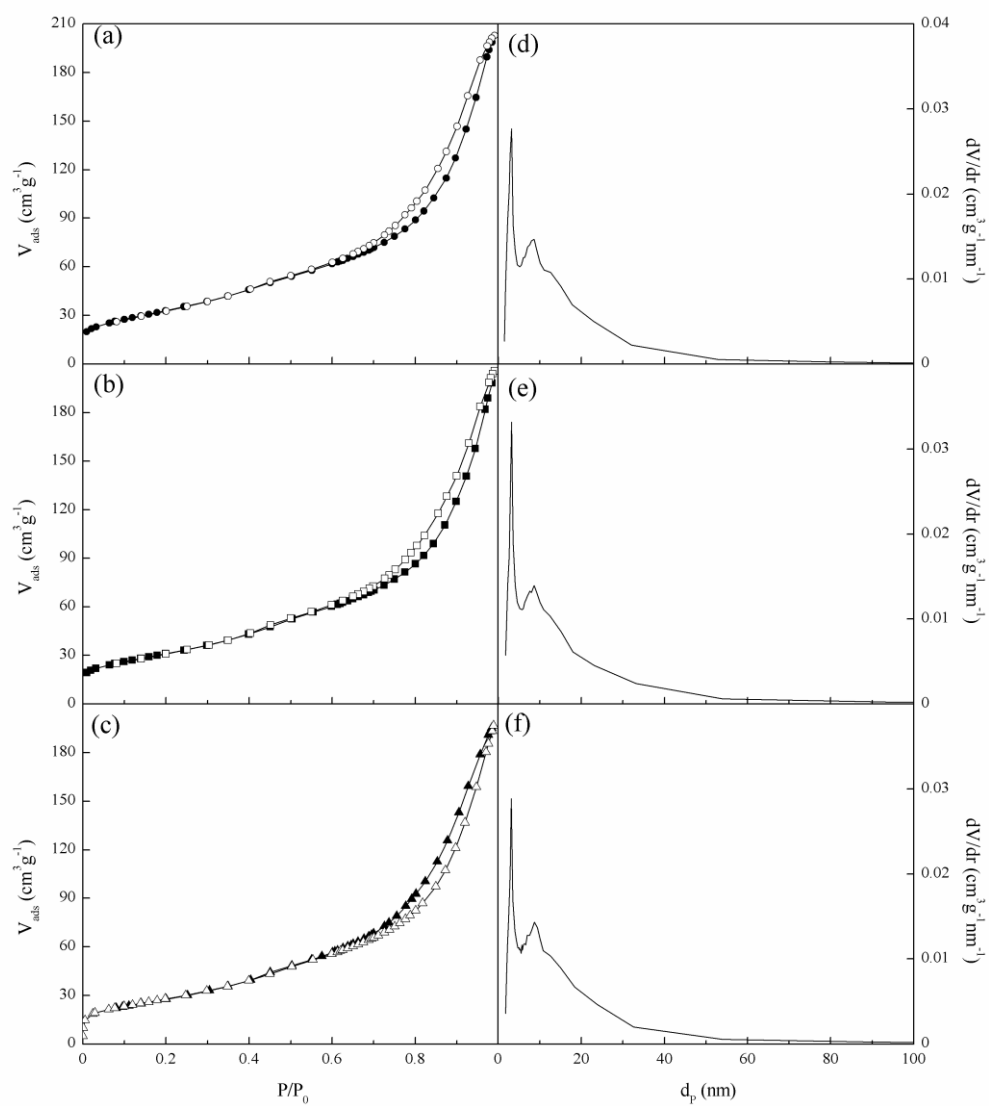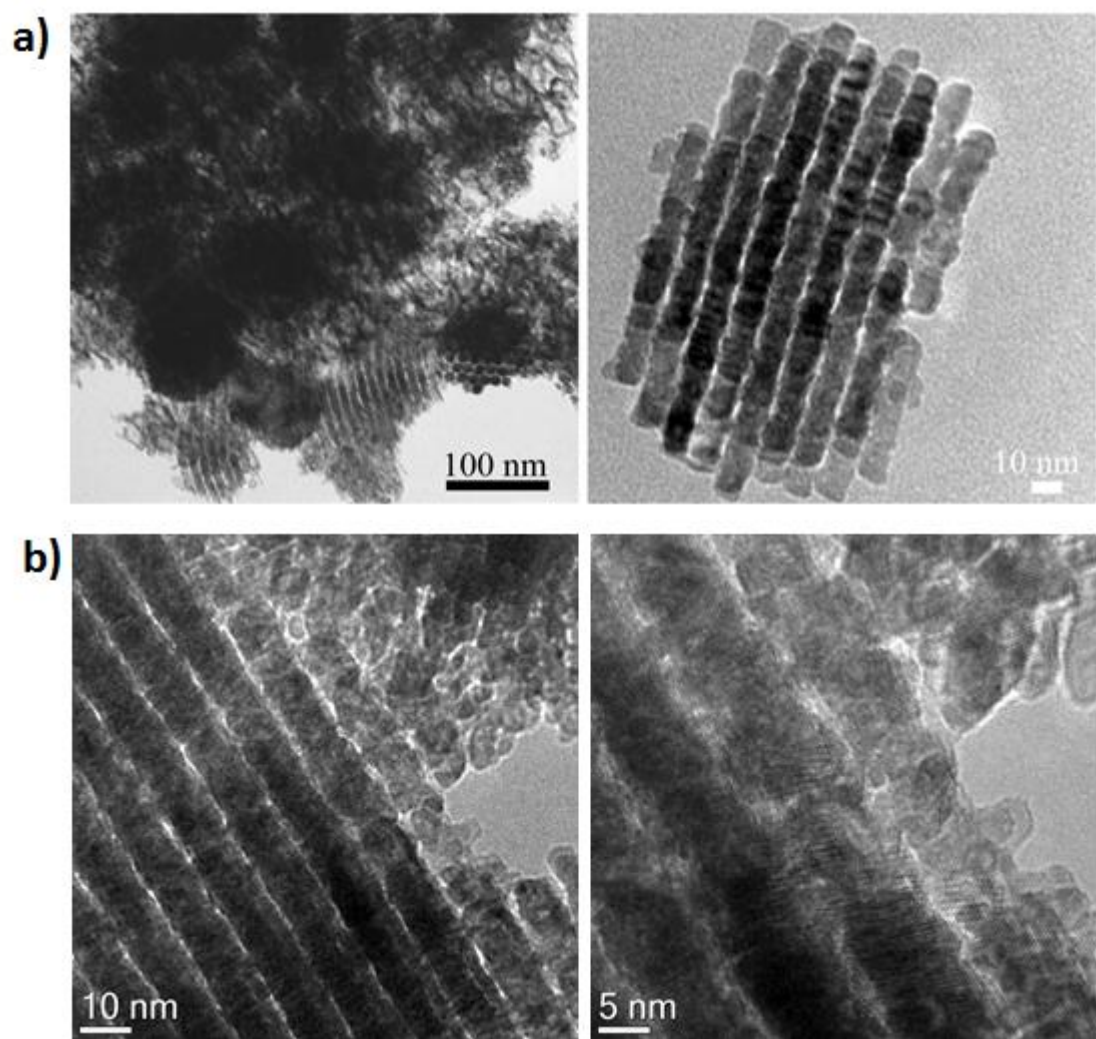
Figure 2

Figure 3

Figure 4

Figure 5

.

a)

b)

Figure 6

33
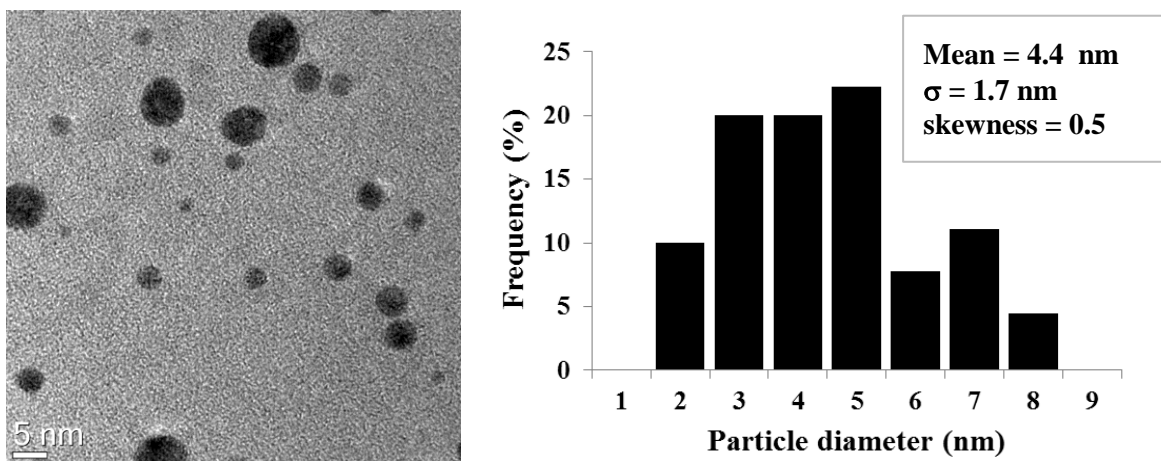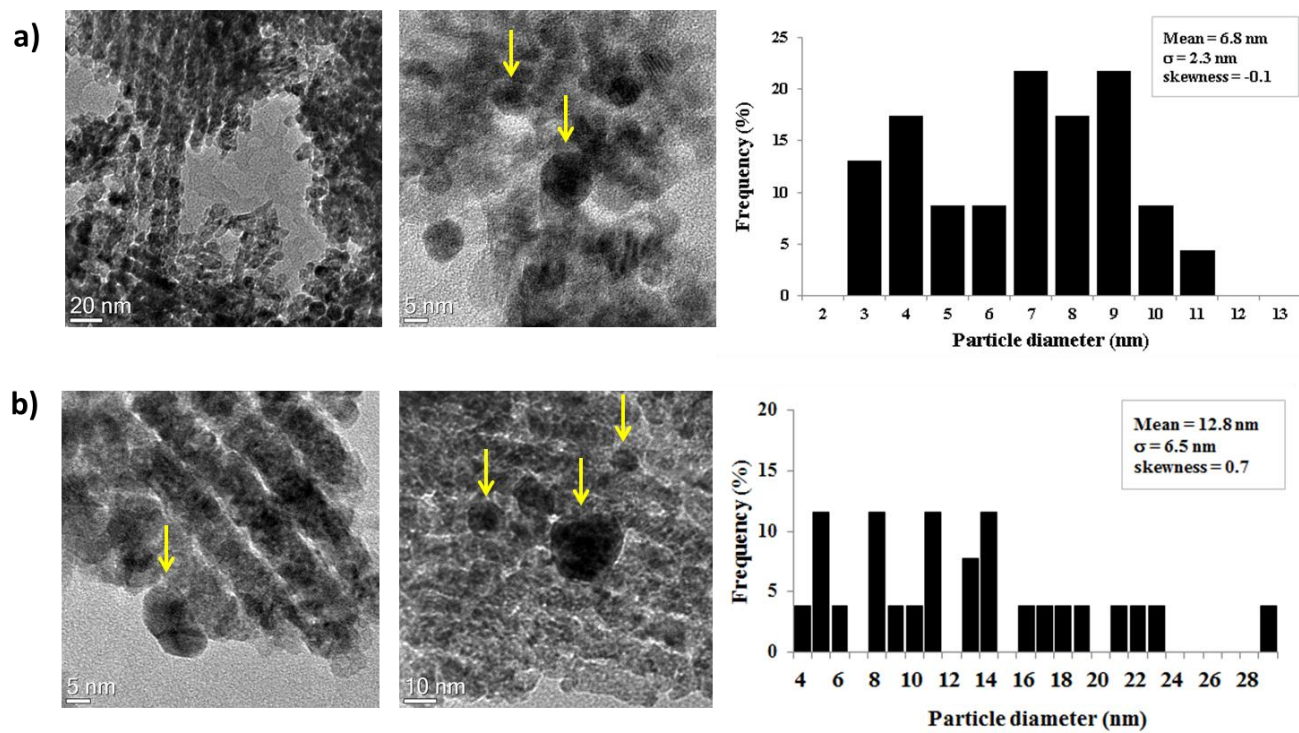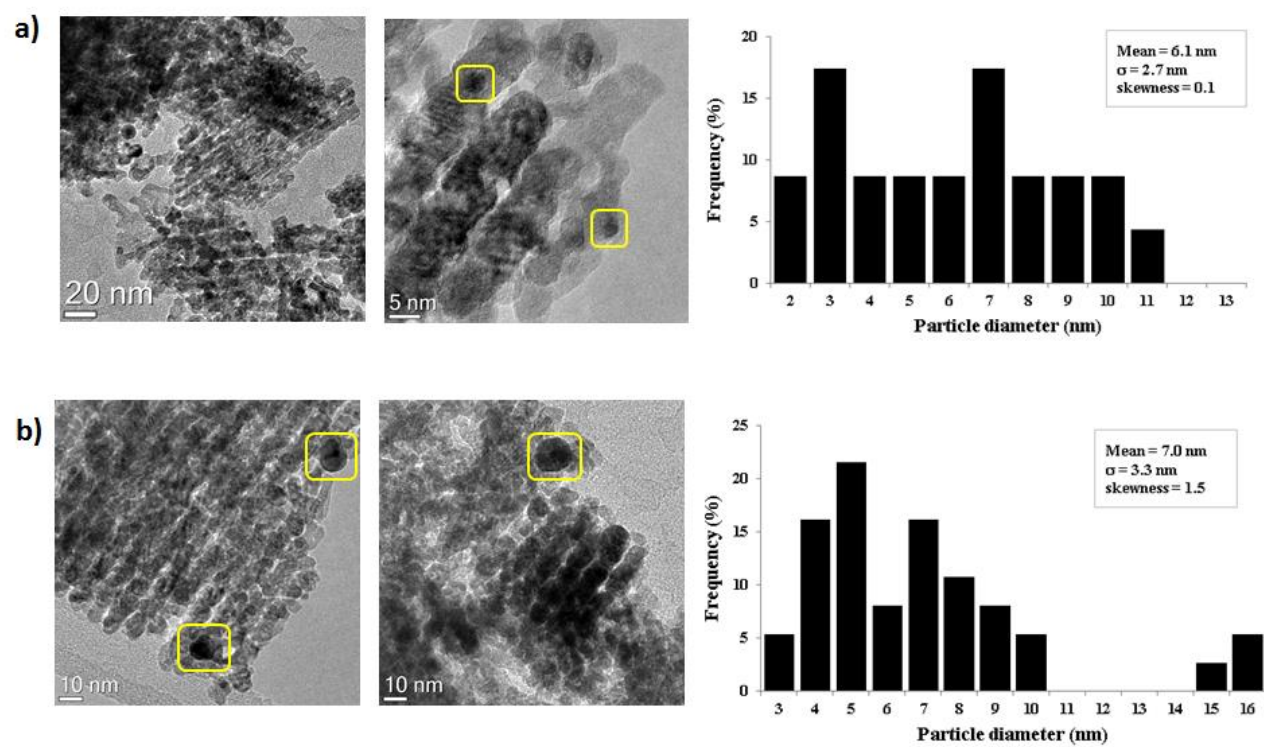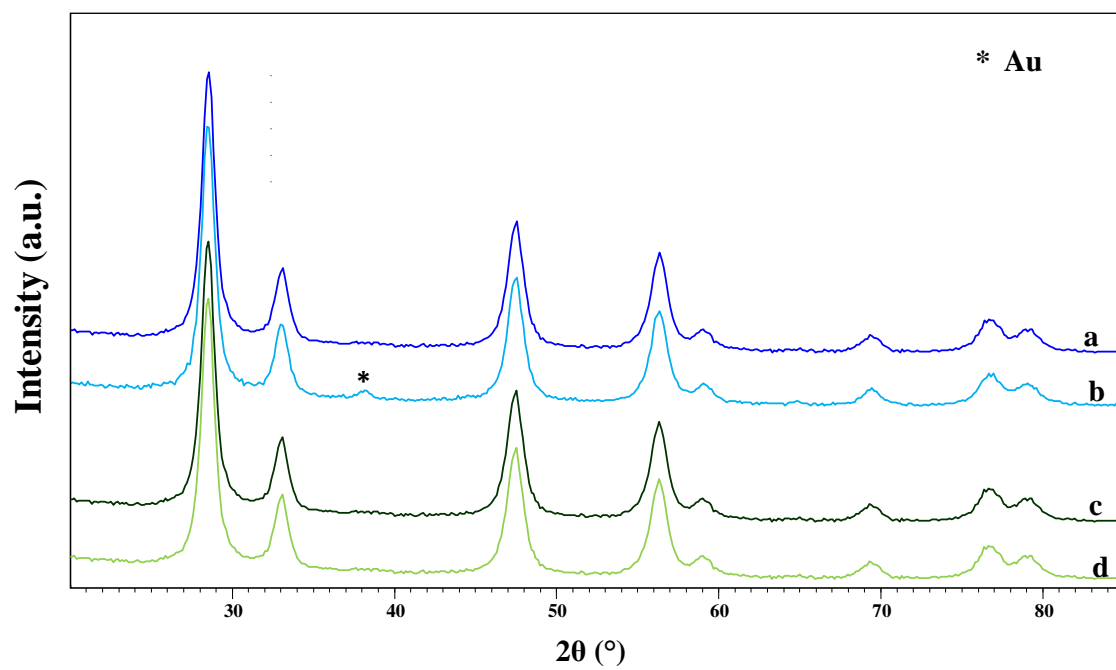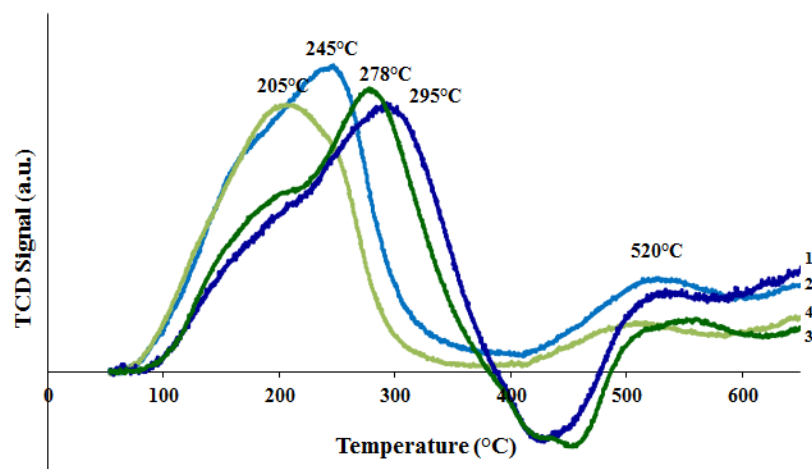
Figure 7

Figure 8

Figure 9

Figure 10

Figure 11